TB, DP, PM/187352, 13/02/2005

INSTITUTE OF PHYSICS PUBLISHING PHYSIOLOGICAL MEASUREMENT

Physiol. Meas. **26** (2005) 1–13 doi:10.1088/0967-3334/26/0/000

A comparison of sensors for minimizing the primary signal in planar-array magnetic induction tomography

S Watson[1], C H Igney[2], O Dössel[2], R J Williams[1] and H Griffiths[3]

[1] School of Electronics, University of Glamorgan, Pontypridd, CF37 1DL, UK
[2] Institut für Biomedizinische Technik, Universität Karlsruhe (TH), Karlsruhe, Germany
[3] Medical Physics and Clinical Engineering, Singleton Hospital, Swansea SA2 8QA, UK

E-mail: swatson1@glam.ac.uk

Received 5 October 2004, accepted for publication 27 January 2005
Published DD MMM 2005
Online at stacks.iop.org/PM/26/1

Abstract

In magnetic induction tomography reducing the influence of the primary excitation field on the sensors can provide a significant improvement in SNR and/or allow the operating frequency to be reduced. For the purposes of imaging, it would be valuable if all, or a useful subset, of the detection coils could be rendered insensitive to the primary field for any excitation coil activated. Suitable schemes which have been previously suggested include the use of axial gradiometers and coil-orientation methods (Bx sensors). This paper examines the relative performance of each method through computer simulation of the sensitivity profiles produced by a single sensor, and comparison of reconstructed images produced by sensor arrays. A finite-difference model was used to determine the sensitivity profiles obtained with each type of sensor arrangement. The modelled volume was a cuboid of dimensions 50 cm $\times$ 50 cm $\times$ 12 cm with a uniform conductivity of 1 S m^{-1}. The excitation coils were of 5 cm diameter and the detection coils of 5 mm diameter. The Bx sensors provided greater sensitivity than the axial gradiometers at all depths, other than on the surface layer of the volume. Images produced using a single-planar array were found to contain distortion which was reduced by the addition of a second array.

Keywords: magnetic induction tomography

1. Introduction

In magnetic induction tomography (MIT) there are two contributions to the signal detected by the sensing coil. The first is directly induced by the field from the excitation coil (the primary signal). The second is from the eddy currents induced within the material, which in turn

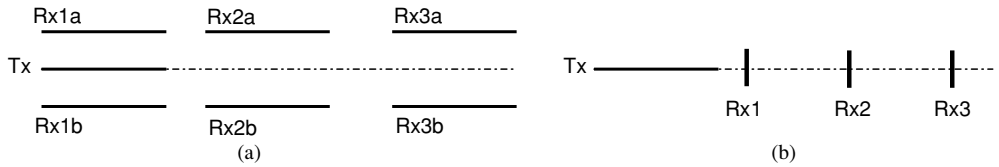

Figure 1. Illustration of minimizing the response to the primary field from a single excitation coil (Tx) for (a) three axial gradiometers (Rx1–Rx3) and (b) three Bx sensors. In each case all three sensors detect no primary signal.

produce their own magnetic field (the eddy-current or secondary signal). The primary signal is often very large in comparison to the eddy-current signal of interest, and is responsible for introducing noise into signal measurements by two means—firstly by restricting the gain which may be applied to the received signal and thereby increasing the contribution of quantization errors, and secondly by introducing phase noise and drift errors in the in-quadrature signal. Minimizing the response of the sensors to the primary field while retaining responsiveness to the eddy-current field can therefore produce very significant improvements in the system's signal to noise ratio and allow it to operate at lower frequencies. A recent review of MIT can be found in Griffiths (2005).

Techniques for minimizing the response to the primary field in multi-channel MIT systems which have been described previously may be categorized into two basic types: symmetry methods (gradiometry) and orientation methods. In symmetry methods, two sensor coils are placed equal distances on either side of any axis of symmetry of the excitation coil. The coils are then connected in serial opposition to produce a gradiometer. Variations on this method include placing the sensor coil pair symmetrically about the plane of the excitation coil to produce an *axial gradiometer* and placing the sensor coil pair symmetrically about the centre axis of the excitation coil to produce a *planar gradiometer* (Rosell *et al* 2001, Scharfetter *et al* 2004). A further technique for minimizing the response of the sensors to the primary field was described by Watson *et al* (2004) in which the sensor coil (termed here a Bx sensor) is placed with its axis oriented normal to the primary field. No net primary flux passes through the sensor coil and it will therefore not detect the primary field.

It would be valuable for a multi-channel imaging MIT system to have a coil array design in which for a given excitation coil, several or all of the detection coils have some measure of response minimization to the primary field. This would allow signal measurements to be performed in parallel, thereby decreasing the total data acquisition time. One array geometry for which multi-channel, primary-field, response minimization is possible is the planar array. The focus of this study was to use a planar array either with axial gradiometers or Bx sensors as detectors (see figure 1). In such a configuration all of the detection coils are insensitive to the primary field no matter which excitation coil is energized.

The objective of this study was to assess the sensitivity distributions of axial gradiometers and Bx sensors to conductivity perturbations within a conducting object and to investigate imaging with a planar array. The following simulation studies were carried out:

(i) The sensitivity distribution with depth was calculated for a single Bx sensor and axial gradiometer.
(ii) Sensor parameters for Bx and axial gradiometers, such as coil diameters, excitation coil–sensor coil distance and excitation coil to sample distance were varied to assess their influence on the sensitivity distribution with depth.
(iii) Images were reconstructed from simulated data from models of planar arrays utilizing Bx sensors.

2. Methods

2.1. Forward model and reconstruction algorithm

The forward modeller was a quasi-static finite-difference algorithm. A three-dimensional volume is divided into cubic voxels with specified conductivity and permittivity. The eddy-current distribution is computed for a given current flowing in a circular excitation coil. The induced emf in a circular detection coil due to the eddy currents is then computed. A full description of the model can be found in Morris *et al* (2001).

To produce the sensitivity matrix S used in image reconstruction a perturbation method was employed with the model iterated to produce the matrix as follows:

1. A value for the background value of conductivity was set for each voxel. The model is then run to determine the signals induced within the detection coil array.
2. A cubic subset of voxels (for this study $4 \times 4 \times 4$ voxels), termed here an *perturbation voxel*, was selected and their conductivity was increased. The model is now run again and the change in the induced signals within the detection coil array, relative to the background conductivity result, is calculated and the result, for all excitation/detection coil combinations, is stored as a single row within the S matrix.
3. Step 2 is then repeated for different image voxels which fill the detector space, e.g. a space discretized into $40 \times 40 \times 20$ calculation voxels will produce $10 \times 10 \times 5$ image voxels if each image voxel is composed of $4 \times 4 \times 4$ calculation voxels. The result of each image voxel result is then stored as a row in the S matrix, producing a S matrix of dimensions *rows* $\times$ *columns* equal to *image voxels* $\times$ *coil combinations*.

Two possible imaging measurements which may be carried out in MIT are (i) *imaging relative to free space* and (ii) *imaging relative to a conductive background*. In each case two measurements sets are acquired by the MIT system. For images relative to free space, a reference measurement set is first acquired with an empty detection volume and the sample is then placed within the detector and the sample measurement set is then acquired. The measurement vector $\mathbf{b}$ will then be the difference in the induced voltages at the detection coils between the two sets for all excitation/detection coil combinations. For images relative to a conductive background the reference set is taken with the sample placed within the detector volume. The measurement vector $\mathbf{b}$ will then be the difference between this and a subsequent set taken with the same sample with perturbation. Imaging relative to free space may be considered to attempt *absolute* imaging while imaging relative to a conductive background produces *difference* imaging.

In this study image reconstruction was performed using two types of sensitivity matrix produced for each of the two cases described above:

- a free space background S matrix. In the calculation of this S matrix the background conductivity was set to zero. The image voxels were then perturbed from 0 S m^{-1} to 1 S m^{-1}.
- a conductive background S matrix. In the calculation of this S matrix the background conductivity of the detection volume was set to 1 S m^{-1}. The image voxels within the volume were then perturbed by 10% from 1 to 1.1 S m^{-1}.

Image reconstruction was carried out utilizing Tikhonov regularization. Considering the MIT forward problem to be described by

$$S\boldsymbol{\sigma} = \mathbf{b} \tag{1}$$

where S is the sensitivity matrix, $\boldsymbol{\sigma}$ is the conductivity distribution vector and $\mathbf{b}$ is the measurement vector, then the Tikhonov regularized solution $\boldsymbol{\sigma}_\lambda$ will be described by the

expression

$$\boldsymbol{\sigma}_\lambda = \min_{\sigma} \left\{ \|S\boldsymbol{\sigma} - \mathbf{b}\|_2^2 + \lambda^2 \|L(\boldsymbol{\sigma} - \boldsymbol{\sigma}_0)\|_2^2 \right\} \tag{2}$$

where $\boldsymbol{\sigma}_0$ is an *a priori* estimate of $\boldsymbol{\sigma}$, L is a regularization matrix and λ is a regularization weighting parameter (Hansen 1994). For this study the identity matrix was used as the regularization matrix and no *a priori* information was incorporated, i.e. $L = I$ and $\boldsymbol{\sigma}_0 = \mathbf{0}$.

To compute the Tikhonov regularized solution $\boldsymbol{\sigma}_\lambda$, the singular value decomposition (SVD) of the sensitivity matrix S was first obtained

$$S = UWV^T = \sum_{i=1}^{n} \mathbf{u}_i \mathbf{w}_i \mathbf{v}_i^T \tag{3}$$

where S has dimension $m \times n$ with $m \geqslant n$, $U = (\mathbf{u}_1, \ldots, \mathbf{u}_n)$ and $V = (\mathbf{v}_1, \ldots, \mathbf{v}_n)$ are matrices with orthonormal columns, T denotes transpose and $w = \mathrm{diag}(w_1, \ldots, w_n)$ with $w_1, \ldots, w_n$ the singular values of S.

Using the SVD the solution to equation (2) may be written in the form (Hansen 1994)

$$\boldsymbol{\sigma}_\lambda = \sum_{i=1}^{n} f_i \frac{\mathbf{u}_i^T \mathbf{b}}{w_i} \mathbf{v}_i . \tag{4}$$

With f_i given by

$$f_i = \frac{w_i^2}{w_i^2 + \lambda^2} \tag{5}$$

if $L = I_n$.

The Tikhonov regularized solution was then computed using equations (4) and (5) employing a MATLAB regularization toolbox (Hansen 1994).

The L-curve method described by Hansen and O'Leary (1993) was utilized for the selection of λ, again employing the MATLAB regularization toolbox. This method provides a rational basis for the choice of an optimal regularization parameter and, through the use of an algorithm for selecting λ by finding the corner of the L-curve, allows automatic selection of λ by the algorithm based on both the sensitivity matrix and the measurement data.

2.2. Single excitor/sensor sensitivity profiles

2.2.1. Comparison of sensitivity with depth for Bx and axial gradiometer sensors. The modelled volume was a tank of 1 S m^{-1} saline of x, y and z dimensions, 50 cm, 50 cm and 12 cm respectively. The volume was split into $100 \times 100 \times 24$ subvoxels for computing the eddy-current density. The excitation coil was a 5 cm diameter, single-turn coil positioned centrally 3 cm below the bottom of the tank at position (0, 0, −9), the origin of co-ordinates being defined as the centre of the tank (cm units). The axis of the coil was in the z-direction (figure 2). The current flowing in the excitation coil was 1 A at a frequency of 1 MHz. The detection coils were (i) a 5 mm diameter single-turn coil with its axis orientated along the x-axis (Bx sensor), positioned at (8, 0, −9) and (ii) an axial gradiometer composed of two 5 mm diameter, single-turn coils with their axes orientated in the z-direction (small gradiometer) and positioned at (8, 0, −8.5) and (8, 0, −9.5).

In order to compute the sensitivity profiles, a perturbation voxel of $4 \times 4 \times 4$ subvoxels was increased in conductivity by 10% and the induced emf at the detection coil due to the perturbation was calculated. The perturbation voxel was positioned initially with its centre at (0, 0, −5), i.e. in layer 1, and was stepped in the positive x-direction by 2 cm at a time in order to obtain the sensitivity profiles. The process was then repeated for $z = -3, -1, 1$

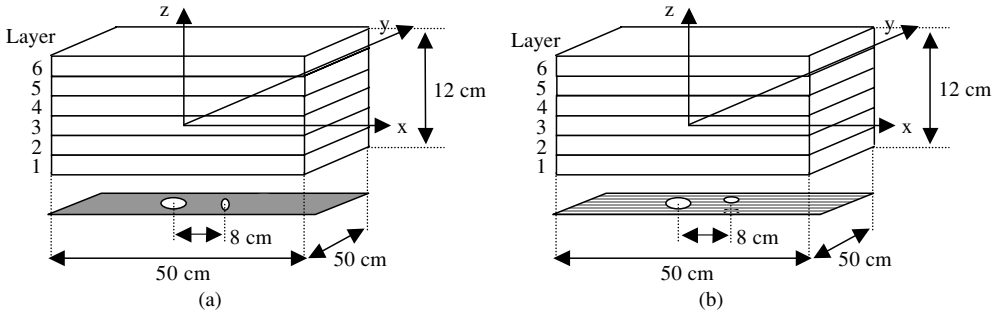

Figure 2. Diagram showing the position of the excitation coil below the conducting tank with (a) a Bx sensor and (b) an axial-gradiometer sensor.

and 3 in order to obtain the profiles for layers 2 to 5. To reduce the influence of boundary effects, treating the volume as approximately a semi-infinite volume, the sensitivity profiles were not computed for positions $x = 21$–25 or for layer 6, with this section of the volume used as 'padding'.

2.2.2. Factors affecting sensitivity with depth. To examine the factors affecting the sensitivity distribution with depth for the axial gradiometers, the above measurements were repeated using an identical simulation volume but with the following variations in the coil parameters:

(i) *Variation in the lateral separation of excitation coil and sensor*. In addition to the lateral separation shown in figure 2, the simulation was performed for a separation of 4 cm, i.e. with the Bx sensor positioned at (4, 0, −9) and the axial gradiometer sensor coil pair positioned at (4, 0, −8.5) and (4, 0, −9.5).
(ii) *Variation in sensor coil diameter*. With the lateral separation of the excitation coil and sensor set at 8 cm, the simulation was carried out for a sensor coil diameter of 5 cm in addition to the 5 mm diameter already stated.
(iii) *Variation in excitation coil diameter*. Again with the lateral separation of the excitation coil and sensor set at 8 cm and the sensor coil diameter set at 5 mm, the simulation was carried out for an excitation coil diameter of 1 cm in addition to the 5 cm diameter.
(iv) *Variation of axial gradiometer sensor coil separation*. For the axial gradiometer a simulation was performed for a sensor coil separation of 0.5 cm (i.e. sensor coil positions (8, 0, −8.75), (8, 0, −9.25)) in addition to the 1 cm separation already stated.
(v) *Variation of coil plane and sample distance*. Initially the centre plane of the coils was positioned at $z = -9$ as shown in figure 2 (dark plane), giving an excitation coil to sample separation of 3 cm. A second set of simulations was carried out with this separation reduced to 1 cm.

2.3. Imaging with planar arrays using Bx sensors

2.3.1. Imaging with a single planar array. The coil array geometry chosen (figure 3) was that adopted for the prototype system described by Riedel *et al* (2004). This comprised a line of four excitation coils (L_{e1-4}), simulated as 5 cm diameter single-turn coils each carrying a current of 1 A at a frequency of 1 MHz, and a line of eight sensor coils (L_{m1-8}) simulated as 5 mm diameter single turn coils. The arrays were positioned 3 cm below the surface of the volume to be imaged, with the centre of the array, marked with an X in figure 3, located at position (0, 0, −8).

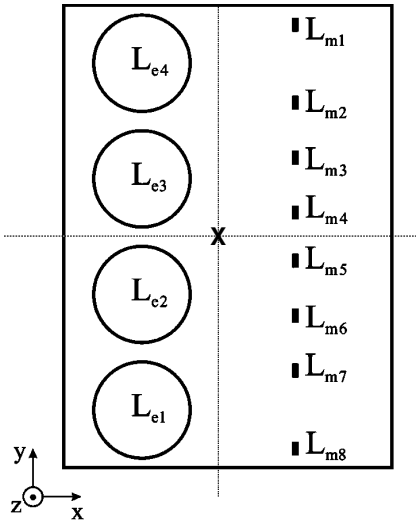

Figure 3. Coil array geometry.

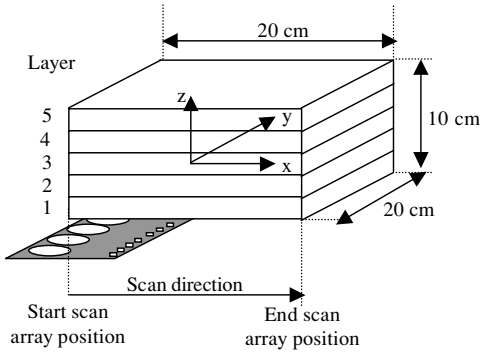

Figure 4. Array scan geometry for single-plane array.

To increase the number of independent measurements available, the arrays were translated in 21 steps of 1 cm in the x-direction to provide $32 \times 21 = 672$ measurements (figure 4). The modelled volume in this case was a tank of x, y and z dimensions, 20 cm, 20 cm and 10 cm respectively. The volume was split into $40 \times 40 \times 20$ subvoxels for computing the eddy-current density. For calculation of the sensitivity matrix, the volume was divided into $10 \times 10 \times 5$ image voxels, each composed of $4 \times 4 \times 4$ subvoxels (i.e. five layers for the purposes of imaging). The free space sensitivity matrix was calculated by setting each image voxel in turn to 1 S m^{-1}, keeping all others as free space. The conductive background sensitivity matrix S_{diff} was calculated as follows:

(i) All voxels in the modelled volume were set to 1 S m^{-1} and a reference measurement vector $\mathbf{b}_{\text{ref}}$ was calculated.
(ii) Each image voxel was in turn set to 1.1 S m^{-1}, keeping all others as 1 S m^{-1}, and the results were stored in a sensitivity matrix S.
(iii) The sensitivity matrix employed for difference imaging S_{diff} was then calculated by subtracting the background measurement $\mathbf{b}_{\text{ref}}$ from each row of S.

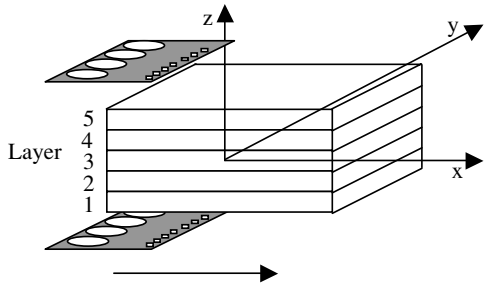

Figure 5. Array scan geometry for two-plane array.

2.3.2. Imaging with two planar arrays. Simulations were undertaken for two planar arrays, one above and one below the volume (figure 5). The first array was positioned as for the simulations of section 2.3.1. A second identical array was added with identical x and y positions, but with its z-position mirrored in the plane $z = 0$, i.e. with its centre (marked X in figure 3) at (0, 0, 8). Both arrays were translated together in 21 steps of 1 cm along the x-axis to provide $32 \times 21 \times 2 = 1344$ measurements. Two sets of simulations were carried, one set with a free space background with image reconstruction utilizing the free space sensitivity matrix, and the other set with a 1 S m^{-1} conductive background with image reconstruction utilizing the conductive background sensitivity matrix.

3. Results

3.1. Comparison of sensitivity with depth for Bx and axial gradiometer sensors

Figures 6(a)–(e) show the sensitivity profiles for the two sensor types on the plane $y = 0$ cm, from $x = 0$ cm to $x = 20$ cm for layers 1–5 respectively. The values for each sensor were normalized to the maximum absolute value obtained in layer 1 for that particular sensor to emphasize the comparative rate of decrease in sensitivity.

The peak induced signals in layer 1 for the Bx sensor and axial gradiometer were 4.1×10^{-10} V and 2.5×10^{-10} V respectively. The rms sensitivity can be used as simple indicator of the information content of the curves as they all contain both positive and negative values. The Bx sensor displayed greater rms sensitivity than the gradiometer at depths into the volume of 1 cm, 3 cm, 5 cm, 7 cm and 9 cm by factors of 1.5, 3, 4, 6 and 7 and for peak sensitivity, factors of 1.6, 3, 5, 7 and 7 respectively. The rms values are quoted with the peak values as a simple measure of the information content of the profiles.

3.1.1. Factors affecting sensitivity with depth. In figures 7(a)–(e), each graph shows the sensitivity profiles for layers 1–5 in the z-direction by plotting the sensitivity versus a 'voxel number' corresponding to the positions $x = 0$ to 19 cm. The voxel numbers were layer 1: voxels numbers 1–20, layer 2: 21–40, layer 3: 41–60, layer 4: 61–80 and layer 5: 81–100.

(i) *Variation in the lateral separation of excitation and sensor coils.* Before normalization, the peak induced signals in layer 1 for the Bx sensor with 4 cm and 8 cm separation were 6.5×10^{-10} V and 3.7×10^{-10} V and for the axial gradiometer were 2.4×10^{-10} and 2.0×10^{-10} V. If the peak normalized signals in each layer are examined (figure 7(a)), it can be seen that increasing the excitation coil/sensor lateral separation from 4 cm to 8 cm for the Bx sensor increased its sensitivity in layers 2–5 by approximately 50–100% (the actual increases in the peak normalized induced signals were 46%, 77%, 98% and 111%

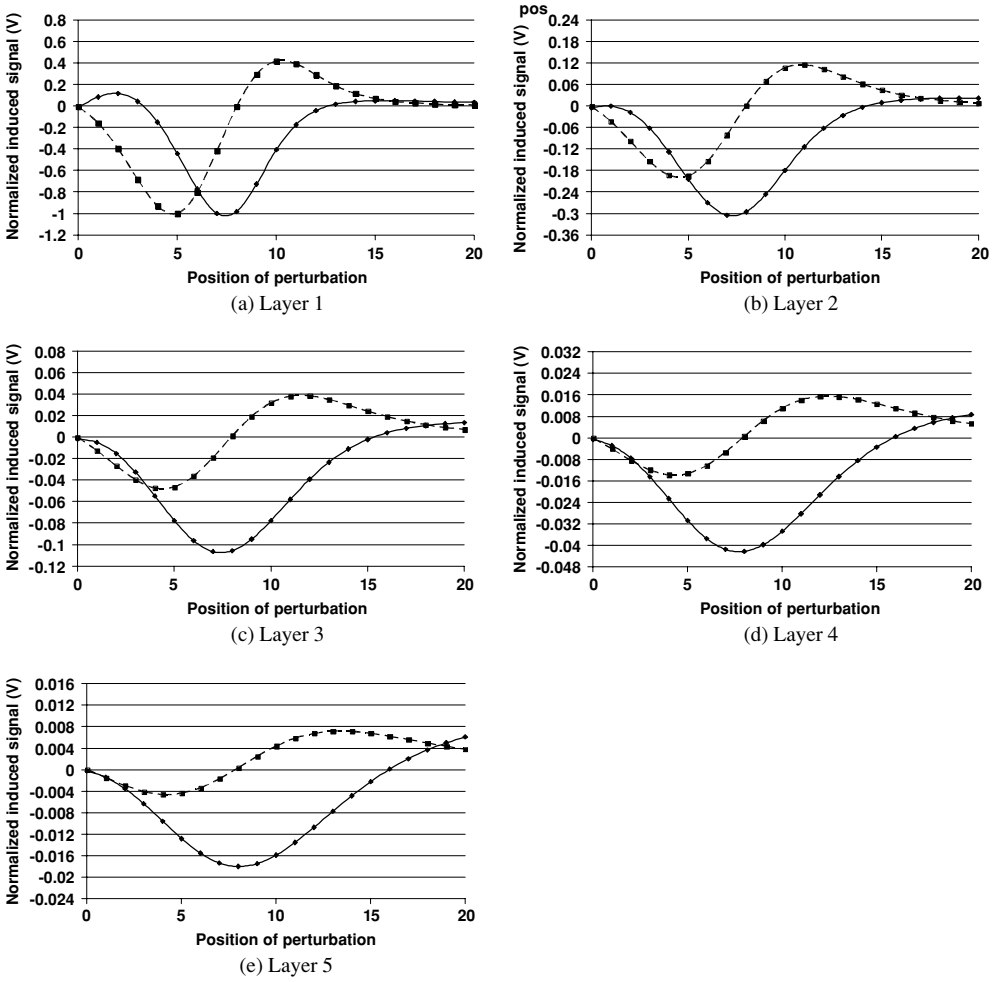

Figure 6. (a)–(e) Sensitivity profiles for Bx sensor (solid line) and axial gradiometer (dashed line). The induced signals for both the Bx sensor and axial gradiometer in each graph have been normalized to the maximum signal obtained in each case within layer 1. The position of the perturbation is the x-coordinate of the centre of the perturbation.

for layers 2, 3, 4 and 5 respectively). For the axial gradiometer, however, no significant increase in depth sensitivity was observed.

(ii) *Variation in sensor coil diameter*. Before normalization, the peak induced signals in layer 1 for the Bx sensor of diameter 5 mm and 5 cm were 3.7×10^{-10} V and 4.6×10^{-8} V respectively and for the axial gradiometer were 2.0×10^{-10} V and 1.6×10^{-8} V. The normalized sensitivity distributions are displayed in figure 7(b). The results suggest that increasing the diameter of the sensor coil increased the overall sensitivity in both Bx sensors and axial gradiometers, but it did not change the sensitivity distribution with depth into the sample for either sensor.

(iii) *Variation in excitation coil diameter*. When the excitation coil diameter was decreased form 5 cm to 1 cm the peak induced signal for the Bx sensor fell from 3.7×10^{-10} to 4.6×10^{-11} V. For the axial gradiometer it fell from 2.0×10^{-10} to 0.8×10^{-11} V.

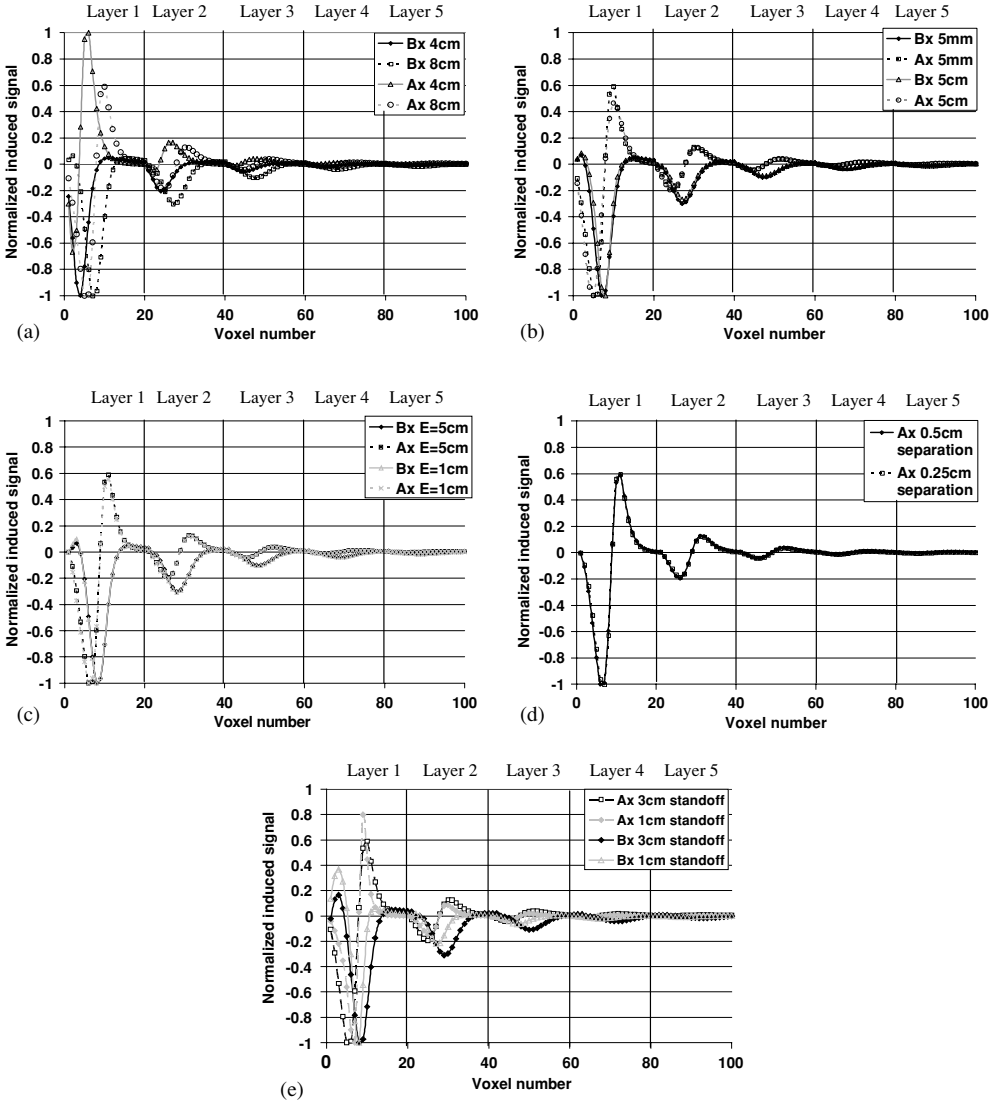

Figure 7. Variation of depth sensitivity for (a) excitation coil/sensor lateral separations of 4 and 8 cm (Ax = axial gradiometer and Bx = Bx sensor), (b) sensor coil radii of 5 mm and 5 cm, (c) an excitation coil radius (E = 1 cm and 5 cm), (d) the axial gradiometer with a sensor coil separation of 0.5 cm and 1 cm and (e) excitation coil to sample distances of 1 cm and 3 cm.

The normalized sensitivity distributions for the two excitation coil radii are displayed in figure 7(c). The results show that although the larger excitation gave a larger absolute sensitivity, the variation of sensitivity with depth into the sample did not change

(iv) *Variation of axial gradiometer sensor coil separation*. Before normalization, the peak induced signal in layer 1 for the axial gradiometer was 2.0×10^{-10} V for a sensor-coil axial separation of 0.5 cm and 2.3×10^{-10} V for a separation of 0.25 cm. The normalized sensitivity distribution with depth are shown in figure 7(d) and reveal negligible change for the two values of separation.

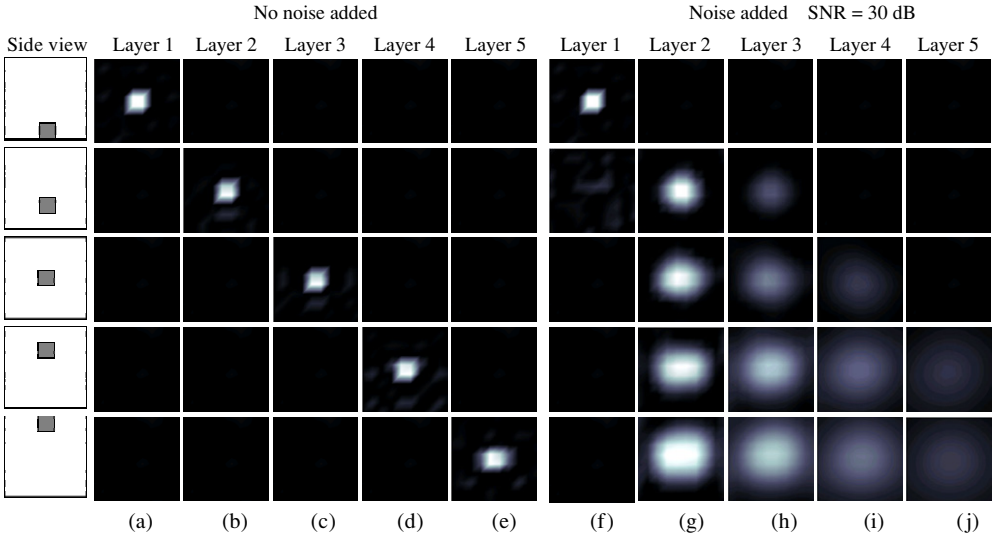

Figure 8. (a)–(j) Reconstructed images using free space sensitivity matrix and the single plane Bx sensor array.

(v) *Variation of coil plane and sample distance*. Before normalization, the peak induced signals in layer 1 for the Bx sensor were 1.7×10^{-9} V and 3.7×10^{-10} V for a coil plane and sample separation distance of 1 cm and 3 cm respectively. For the axial gradiometer the values were 1.4×10^{-9} V and 2.0×10^{-10} V. The normalized sensitivity distributions with depth are given in figure 7(e) and show that for both types of sensor the normalized sensitivities in layers 2 and 5 were increased by the order of 25% as the stand-off was increased from 1 cm to 3 cm.

3.2. Reconstructed images from simulated data

Figures 8(a)–(j) show the reconstructed images from the simulation of a 2 cm cube (one perturbation voxel) of 1 S m^{-1} in free space for the single array. Figures 8(a)–(e) demonstrate the behaviour of the reconstruction algorithm with the sample placed at varying heights above the array and were produced with the cube placed at $z = -4, -2, 0, 2$ and 4 respectively, with $x = 0$ and $y = 0$ for all five simulations (axes as shown in figure 1(a)). No noise was added to the simulated data in these reconstructions. Figures 8(f)–(j) were reconstructed from the same simulated data sets as 8(a)–(e) respectively, but with Gaussian noise added to the data with a SNR of 30 dB. The SNR figure employed for all the images was calculated relative to the peak simulated value obtained with the perturbation placed in layer 3, allowing the same level of noise to be applied to all of the reconstructions. Now, the image of the perturbation appears blurred and displaced back towards the array.

Simulations of a 1.1 S m^{-1} perturbation placed in a 1 S m^{-1} background were now carried out and the images were reconstructed using the conductive background sensitivity matrix. The perturbation dimensions and positions were identical to that employed for the images shown in figure 8(a)–(j). Figures 9(a)–(e) show the reconstructed images obtained with no noise added, while Figures 9(f)–(j) show the results obtained when an identical level of noise was added to the data as for figures 8(f)–(j). Again the introduction of noise can be seen to

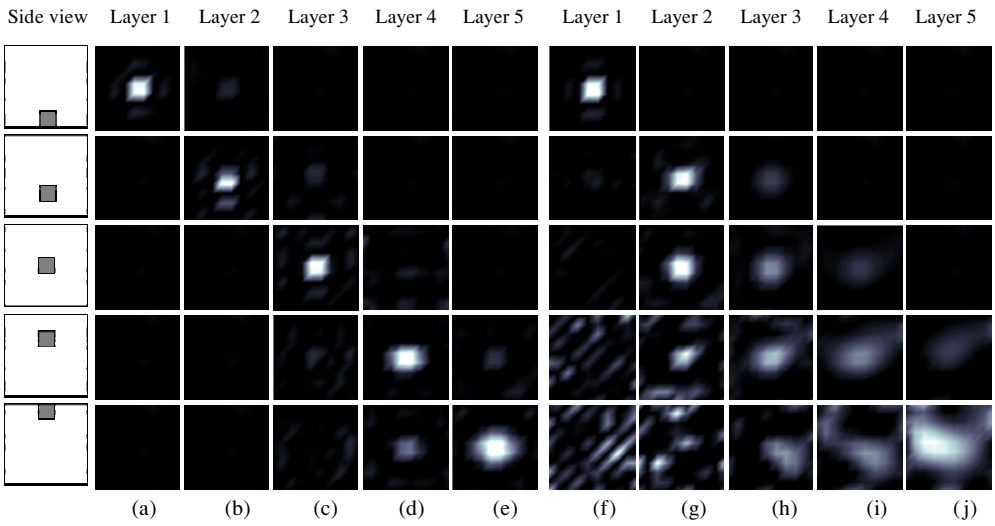

Figure 9. (a)–(j) Reconstructed images using conductive background sensitivity matrix and the single plane Bx sensor array.

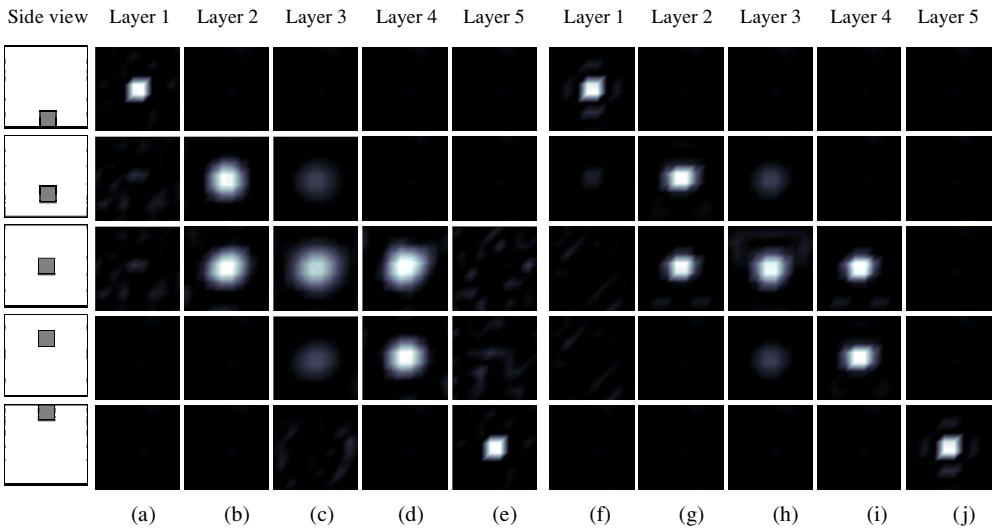

Figure 10. Reconstructed images obtained using a two plane Bx sensor array with (a)–(e) for a 1 S m^{-1} perturbation in a free space background, and (f)–(j) for a 1.1 S m^{-1} perturbation in a 1 S m^{-1} background.

degrade the localization of the perturbation in the z-direction with compression of the image back towards the array.

Figure 10 shows the results obtained with the double array using an identical 2 cm cube sample, with the same 30 dB noise level as before added to the measurements. Figures 10(a)–(e) were reconstructed using a 1 S m^{-1} perturbation in free space, while figures 10(f)–(j) were obtained for a 1.1 S m^{-1} perturbation in a 1 S m^{-1} background. In both cases the cube

can now be seen to be correctly localized in layers 4 and 5, but the array still produces poor z-direction localization in layer 3.

4. Discussion

Minimizing the magnitude of the primary signal is likely to be essential for biomedical MIT. The relatively low contrast between tissue types and the small changes in tissue electrical impedance, which are required to be resolved in potential biomedical applications such as the detection of oedema in the brain (Merwa *et al* 2004), chest and limbs, requires a high signal to noise ratio in the measurements. The characteristic frequencies associated with the β-dispersion in biological tissues are typically in the range 10 kHz to 1 MHz and sufficient contrast between normal and abnormal tissue states, due to oedema or ischaemia for instance, may only be available within this frequency range. MIT systems without primary signal minimization are unlikely to provide adequate SNR below 1 MHz.

A planar array design is relatively simple and may provide practical advantages in terms of mechanical stability. It also provides an 'open' detection volume which could be attractive for some biomedical applications, in particular in long-term monitoring. Two possible sensor types which are suitable for use in a planar array are axial gradiometers and Bx sensors. The results presented in figure 6 suggest that the Bx sensor provided better sensitivity at depth than the axial gradiometer and may be the most suitable sensor for measurements of electrical impedance within one excitation coil radius into the sample. If on the other hand surface measurements are required, with the depth sensitivity limited to the surface layer, then the axial gradiometer appears to be more suitable. The results displayed in figure 7 suggest that the depth sensitivity may be manipulated for the Bx sensor by varying the lateral separation of the excitation and sensor coils, or by varying the excitation coil and sample distance. For the axial gradiometer, only variation of the excitation coil and sample distance affected the depth sensitivity distribution. Although varying the dimensions of the excitation and sensor coils independently did not affect the depth sensitivity distribution, it is obvious that changes in scale, i.e. reducing or increasing all of the dimensions of the coil array and the array–sample distance together, will influence depth sensitivity.

A further point which must be considered however is the comparative performance of each sensor type as regards noise and drift in practical implementations. Scharfetter *et al* (2004) highlighted the greater immunity to distant external noise sources provided by gradiometers in comparison to Bx sensors, with Bx sensors requiring effective electromagnetic screening to match the noise performance of gradiometers. The small dimensions and simpler design of Bx sensors may provide advantages as regards thermally/mechanically induced drift however, and a comparative study of practical implementations of arrays of both types is required. Such drift in principle affects the real signal component primarily, with sensor misalignments resulting in increased sensitivity to the primary field for both sensor types. The use of phase sensitive detection with accurate determination of the real and imaginary signal components should therefore reduce the influence of such drift on measurements of the conductivity of samples for which the imaginary component is of interest. However, reducing overall drift by optimizing the mechanical stability of the sensors and arrays is desirable.

The images presented in figure 9 show that at realistic noise levels planar arrays display image distortion with the image compressed back towards the array. This form of image distortion is also found in annular arrays, and has been associated with higher weighting of lower singular value basis images close to the array transducers (Zadehkoochak *et al* 1991). This may be addressed to some extent by using two or more planes as shown in the results displayed in figure 10. Poor localization due to low sensitivity within central

regions of the volume is still a major problem however. It should be noted that the SNR employed in reconstructing the images in figures 8, 9 and 10 was of the order of 30 dB higher than that obtained with the prototype Bx-sensor planar array MIT system reported by Riedel *et al* (2004)—the single-plane system which was simulated for figures 8 and 9. A significant improvement in the measurement precision of this device would therefore be required for this system to provide the image reconstruction performance, for low-contrast ($\sim$10%) perturbations of small dimensions ($\sim$2 cm), demonstrated in these images.

In conclusion, planar arrays appear to provide useable measurement sensitivity, at least as regards the distribution of the sensitivity with depth, into volumes up to a depth limit of the order of the radius of the excitation coil employed, and possibly double this for the 'sandwich' method using two planar arrays. Bx sensors provide higher sensitivity at depth than axial gradiometers. If measurements are to be restricted to surface layers, e.g. measurements of the electrical impedance of epithelium, then a small axial gradiometer placed as close to the surface as possible is indicated. For the cross-sectional imaging of objects with approximately cubic, spherical or cylindrical volumes such as the head or limbs, annular arrays however are likely to provide a more effective design, with higher sensitivity and image resolution within central regions.

References

Griffiths H 2005 *Magnetic induction tomography. Electrical Impedance Tomography: Methods, History and Applications* (Bristol: Institute of Physics Publishing) pp 213–38

Hansen P C 1994 RegularizationTools: A Matlab package for analysis and solution of discrete ill-posed problems *Numer. Algorithms* **6** 1–35

Hansen P C and O'Leary D P 1993 The use of the L-curve in the regularisation of discrete ill-posed problems *SIAM J. Sci. Comput.* **14** 1487–503

Merwa R, Hollaus K, Oszkar B and Scharfetter H 2004 Detection of brain oedema using magnetic induction tomography: a feasibility study of the likely sensitivity and detectability *Physiol. Meas.* **25** 347–54

Morris A, Griffiths H and Gough W 2001 A numerical model for magnetic induction tomographic measurements in biological tissues *Physiol. Meas.* **22** 113–9

Riedel C H, Watson S, Griffiths H, Williams R J and Dössel O 2004 Design and performance of a planar array MIT system *Proc. 12th Int. Conf. Electrical Bioimpedance and V Electrical Impedance Tomography (Gdansk, PL, June 20–24, 2004)*

Rosell J, Casanas R and Scharfetter H 2001 Sensitivity maps and system requirements for magnetic induction tomography using a planar gradiometer *Physiol. Meas.* **22** 121–30

Scharfetter H, Rauchenzauner S, Merwa R, Biró O and Hollaus K 2004 Planar gradiometer for magnetic induction tomography (MIT): Theoretical and experimental sensitivity maps for a low-contrast phantom *Physiol. Meas.* **25** 325–33

Watson S, Morris A, Williams R J, Griffiths H and Gough W 2004 A primary field compensation scheme for planar array magnetic induction tomography *Physiol. Meas.* **25** 271–9

Zadehkoochak M, Blott B H, Hames T K and George R F 1991 Spectral expansion analysis in electrical-impedance tomography *J. Phys. D Appl. Phys.* **24** 1911–6